

THE PROPERTIES OF MICROJANSKY RADIO SOURCES IN THE HDF-N, SSA13, AND SSA22 FIELDS

S. C. CHAPMAN,¹ A. J. BARGER,^{2,3,4} L. L. COWIE,⁴
D. SCOTT,⁵ C. BORYS,⁵ P. CAPAK,⁴ E. B. FOMALONT,⁶ G. F. LEWIS,⁷ E. A. RICHARDS,⁸
A. T. STEFFEN,² G. WILSON,⁹ M. YUN¹⁰

Submitted to The Astrophysical Journal

ABSTRACT

We present multiwavelength observations for a large sample of microjansky radio sources detected in ultradeep 1.4 GHz maps centered on the Hubble Deep Field-North (HDF-N) and the Hawaii Survey Fields SSA13 and SSA22. Our spectroscopic redshifts for 169 radio sources reveal a flat median redshift distribution, and these sources are hosted by similarly luminous optical L^* galaxies, regardless of redshift. We suggest that the absence of low optical luminosity galaxies at low redshifts, where there are no selection effects, is due to small galaxies not being efficient at retaining the cosmic rays necessary to host microjansky radio sources. This is a serious concern for radio estimates of the local star formation rate density, as a substantial fraction of the ultraviolet luminosity density is generated by sub- L^* galaxies at low redshifts. From our submillimeter measurements for 278 radio sources, we find error-weighted mean 850 μm fluxes of 1.72 ± 0.09 mJy for the total sample, 2.37 ± 0.13 mJy for the optically-faint ($I > 23.5$) subsample, and 1.04 ± 0.13 mJy for the optically-bright ($I < 23.5$) subsample. We significantly ($> 3\sigma$) detect in the submillimeter 50 of the radio sources, 38 with $I > 23.5$. Spectroscopic redshifts for three of the $I < 23.5$ submillimeter-detected radio sources are in the range $z = 1.0$ – 3.4 , and all show AGN signatures. Using only the submillimeter mapped regions we find that $69 \pm 9\%$ of the submillimeter-detected radio population are at $I > 23.5$. We also find that $66 \pm 7\%$ of the $S_{850 \mu\text{m}} > 5$ mJy ($> 4\sigma$) sources are radio-identified. We use our spectroscopic sample to determine the evolution with redshift of the radio power, and hence the far-infrared (FIR) luminosity (through the local FIR-radio correlation). We find that millimetric redshift estimates at low redshifts are best made with a FIR template intermediate between a Milky Way type galaxy and a starburst galaxy, and at high redshifts with an Arp 220 template.

Subject headings: cosmology: observations — galaxies: evolution — galaxies: formation — galaxies: starburst

1. INTRODUCTION

Some of the deepest 1.4 GHz maps ever obtained with the Very Large Array (VLA) are centered on the Hubble Deep Field-North (HDF-N) and the Hawaii Survey Fields¹¹ SSA13 and SSA22. These maps should be sensitive to the synchrotron emitting disks of galaxies out to $z \sim 1$ and the nuclear starbursts of ultraluminous infrared galaxies (Sanders & Mirabel 1996) out to $z \sim 3$. Most importantly, since 1.4 GHz emission does not suffer from absorption by galactic dust or neutral hydrogen at high redshifts, even the most distant, dust-obscured galaxies should be transparent. The 1.4 GHz maps of the HDF-N, SSA13, and SSA22 fields are not only unprecedented in their sensitivities (e.g., the r.m.s. of the SSA13 image is 5 μJy) but also in their detailed resolution, which has

enabled unambiguous optical identifications to be made on images aligned to within $0.1'' - 0.2''$ of the radio FK5 coordinate grid. These optical identifications are composed of 10%–20% late-type Seyfert galaxies and bright field elliptical galaxies and 60%–70% moderate redshift ($0.1 < z < 1.3$) starburst galaxies characterized by their diffuse synchrotron emission on galactic scales ($1'' - 2''$; T. W. B. Muxlow et al., in preparation). The remainder of the sources are unidentified to $I \sim 25$. Thus, the faint radio source population appears to be dominated by moderate-redshift star-forming galaxies (e.g., Windhorst et al. 1995; Richards 2000).

Sensitive submillimeter follow-up observations with the Submillimetre Common User Bolometer Array (SCUBA; Holland et al. 1999) on the 15 m James Clerk Maxwell Telescope¹² of the optically-faint tail of the radio source

¹California Institute of Technology, Pasadena, CA 91125

²Department of Astronomy, University of Wisconsin-Madison, Madison, WI 53706

³Department of Physics and Astronomy, University of Hawaii, Honolulu, HI 96822

⁴Institute for Astronomy, University of Hawaii, Honolulu, Hawaii 96822

⁵Department of Physics & Astronomy, University of British Columbia, Canada V6T 1Z1

⁶National Radio Astronomy Observatory, Charlottesville, VA 22903

⁷Anglo-Australian Observatory, P.O. Box 296, Epping, NSW 1710, Australia

⁸University of Alabama, Huntsville, AL 35899

⁹Physics Department, Brown University, Providence, RI 02912

¹⁰University of Massachusetts, Department of Astronomy, Amherst, MA 01003

¹¹Central coordinates: $13^{\text{h}}12^{\text{m}}35^{\text{s}}.2, 42^{\circ}44'24''$ (SSA13) and $22^{\text{h}}17^{\text{m}}59^{\text{s}}.2, 00^{\circ}18'31''$ (SSA22); Cowie et al. (1996).

¹²The JCMT is operated by the Joint Astronomy Centre on behalf of the parent organizations the Particle Physics and Astronomy Research

population have revealed significant numbers of $S_{850\ \mu\text{m}} > 5\ \text{mJy}$ sources (Barger, Cowie, & Richards 2000, hereafter BCR00; Chapman et al. 2001, hereafter C01; Chapman et al. 2002a, hereafter C02) whose submillimeter emission appears to be produced primarily by star formation rather than by accretion onto supermassive black holes (Barger et al. 2001a, b).

A radio selection technique can therefore be used to identify bright submillimeter sources without the need for long submillimeter exposures. C01 found that high-redshift $S_{850\ \mu\text{m}} > 5\ \text{mJy}$ sources can be detected with SCUBA in photometry mode at a rate of about one per hour, which is significantly more rapid than the rate of about one per 10 hours achieved in blank-field jiggle map surveys (e.g., Barger et al. 1998; Hughes et al. 1998). Moreover, the $S_{850\ \mu\text{m}}/S_{1.4\ \text{GHz}}$ ratio can be used as a millimetric redshift indicator (Carilli & Yun 1999, 2000, hereafter CY99 and CY00; BCR00; Dunne, Clements, & Eales 2000, hereafter DCE00). Millimetric redshift estimates of submillimeter-detected radio sources are typically in the range $1 < z < 3$ (e.g., BCR00; Smail et al. 2000; C01; C02; Ivison et al. 2002).

Flux-limited radio selection does introduce a luminosity bias with redshift (see § 5.1); even very sensitive radio maps, such as those used in the present paper, will not detect galaxies at very high redshifts. C02 modeled the radio selection function in detail using different galaxy evolution scenarios and found that the primary bias was a cut-off of galaxies at $z \lesssim 3$ due to the radio sensitivity, although the specific form of galaxy evolution and dust properties also affected the radio-detectable sources. However, the large percentage ($\sim 70\%$; see § 4.3) of $S_{850\ \mu\text{m}} > 5\ \text{mJy}$ blank-field counts recovered through radio selection shows that most of the bright submillimeter sources can be found this way, in agreement with predictions from the C02 best-fit models.

Although microjansky radio sources have proved to be a crucial resource for identifying and studying the nature of submillimeter-luminous galaxies, the submillimeter-detected samples are only a small fraction of the radio population. In this paper we present multiwavelength observations of a large sample of microjansky radio sources detected in ultradeep 1.4 GHz maps of the HDF-N, SSA13, and SSA22 fields to learn about the nature and evolution with redshift of the microjansky radio population, as well as the implications of using this population to study the bright submillimeter source population. We assume a flat $\Omega_\Lambda = 2/3$ Universe with $H_0 = 65\ \text{km s}^{-1}\ \text{Mpc}^{-1}$.

2. OBSERVATIONS

2.1. Radio imaging

Data at 1.4 GHz were obtained for the HDF-N, SSA13, and SSA22 fields using the VLA. The HDF-N radio map (Richards 2000) was observed in the A-array configuration, resulting in an $\sim 1.5''$ beam and reaching a sensitivity of $40\ \mu\text{Jy}$ (5σ). The SSA13 radio map (E. B. Fomalont et al., in preparation) was observed in both the A and B-array configurations for a total of 100 hours, resulting in

an $\sim 1.5''$ beam and reaching a sensitivity of $25\ \mu\text{Jy}$ (5σ). The SSA22 radio map (M. Yun et al., in preparation) was observed in the B-array configuration for 12 hours, resulting in an $\sim 5''$ beam and reaching a sensitivity of $60\ \mu\text{Jy}$ (5σ).

2.2. Optical and near-infrared imaging

Deep *I*-band imaging was used to identify the radio sources. The *I*-band image of the HDF-N field was obtained with the Subaru Prime Focus Camera (Suprime-Cam; Miyazaki et al. 1998) on the 8.2 m Subaru¹³ telescope. Details of the observations and reductions can be found in Barger et al. (2002), and catalogs of all the galaxies and stars in the field are presented in P. Capak et al., in preparation. The HDF-N optical image covers $24' \times 24'$ to $I = 25.8$ (5σ). In the HDF-N field, 357 radio sources have *I*-band measurements.

The *I*-band image of the SSA13 field (Barger et al. 2001a) was formed from a mosaic of overlapping images obtained with the Low Resolution Imaging Spectrograph (LRIS; Oke et al. 1995) on the 10 m Keck¹⁴ telescopes. In the SSA13 field, 145 radio sources have *I*-band measurements.

The *I*-band image of SSA22 was obtained with the CFH12K camera (Cuillandre et al. 2000) on the 3.6 m Canada-France-Hawaii Telescope (CFHT). The 8.1 hour integration reaches $I = 26.1$ (5σ). Details are presented in S. C. Chapman et al., in preparation. In the SSA22 field, 122 radio sources have *I*-band measurements.

For $I > 21$ we used $3''$ diameter aperture measurements corrected to total magnitudes using an average median offset. For $I < 21$ we used isophotal magnitudes measured to 1% of the peak surface brightness of each galaxy. Isophotal magnitudes provide a better measure of the total magnitudes in these generally low redshift galaxies with extended angular sizes.

Deep *K*-band imaging of SSA22 was obtained at UKIRT using the UKIRT Fast Track Imager (UFTI). The small UFTI field ($50'' \times 50''$) was centered on the positions of the $> 3\sigma$ submillimeter-detected radio sources. Each source was imaged for a total of 3600 s using individual exposures of 60 s; the limiting magnitude in a $2''$ diameter aperture is $K = 20.8$ (5σ). The fast tip/tilt, adaptively-corrected imaging resulted in seeing better than the median conditions of $0.45''$ FWHM. The data were reduced using the Starlink UKIRT/UFTI image processing tools under the ORACDR environment (Bridger et al. 2000). We wrote custom ORACDR scripts to optimize point-source sensitivity in our essentially blank-field observations, creating flat-fields from each 9-point dither and high signal-to-noise thermal background images from 60 minutes of data.

For sources in the HDF-N, *K*-band magnitudes were inferred from the deep *HK'* image of the Hubble Flanking Fields (Barger et al. 1999; $HK' - K = 0.3$) obtained using the University of Hawaii Quick Infrared Camera (QUIRC; Hodapp et al. 1996) on the 2.2 m University of Hawaii telescope and the CFHT. The image reaches an effective limiting magnitude of $K = 20.1$ (5σ).

Council in the United Kingdom, the National Research Council of Canada, and the Netherlands Organization for Scientific Research.

¹³The Subaru telescope is operated by the National Astronomical Observatory of Japan

¹⁴The W. M. Keck Observatory is operated as a scientific partnership among the California Institute of Technology, the University of California, and NASA, and was made possible by the generous financial support of the W. M. Keck Foundation

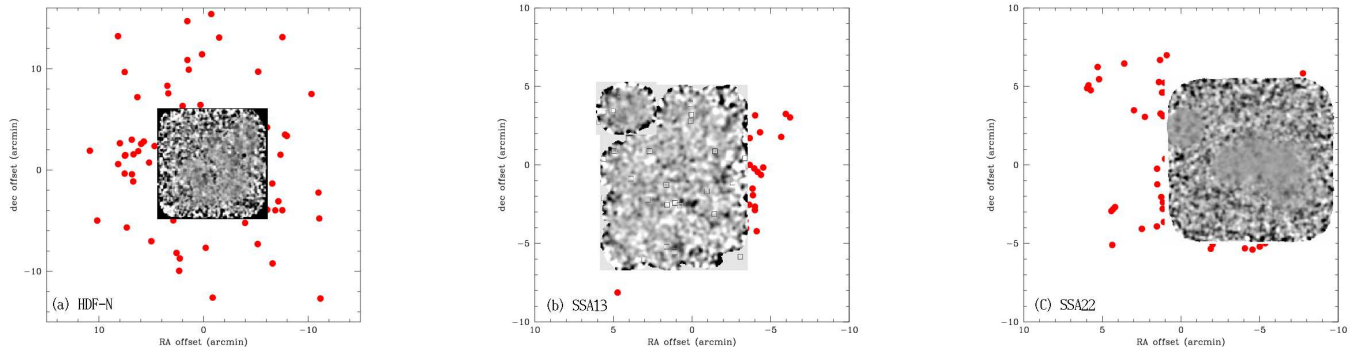


FIG. 1.— Configuration of the submillimeter data in the HDF-N, SSA13, and SSA22 fields (as indicated in panels a,b,c). A central area of ~ 120 arcmin² has been mapped with SCUBA to a uniform depth of ~ 2 mJy in all three fields, although small subregions go much deeper. For illustration, we have indicated the radio sources with squares within the field with the deepest radio map (SSA13). Targeted submillimeter follow-up of $I > 23.5$ radio sources was undertaken outside of the SCUBA mapped regions, but within the VLA primary beam (shown with filled circles), as well as within the SCUBA mapped regions to confirm map detections. The half-power point of the VLA primary beam at 1.4 GHz is $30'$ diameter.

2.3. Optical spectroscopy

Spectroscopic measurements of 158 radio sources in the HDF-N and 51 in the SSA13 field were made with LRIS on Keck and with the HYDRA spectrograph (Barden et al. 1994) on the 3.5 m WIYN telescope. *We hereafter refer to the radio sources in the HDF-N and SSA13 fields with spectroscopic measurements as our spectroscopically-observed radio sample.* Redshift identifications were obtained for 169 sources: 126 in the HDF-N and 43 in SSA13. The spectral observations and reductions are presented and described in BCR00 and E. B. Fomalont et al., in preparation (see also Cohen et al. 2000 and Barger et al. 2002 for many of the redshifts in the HDF-N field).

2.4. Submillimeter imaging

The submillimeter data were taken in SCUBA jiggle map, SCUBA raster map, or SCUBA photometry mode at $850 \mu\text{m}$ during a number of observing runs with good to excellent conditions. The configuration of the data in all three fields is similar: a roughly $10' \times 10'$ region in the center of the $40'$ diameter VLA primary beam was mapped with SCUBA in either jiggle map or raster map mode to an average sensitivity of 2 mJy r.m.s. (with small subregions reaching as deep as 0.5 mJy r.m.s.). These maps present an unbiased study of the submillimeter properties of the microjansky radio sources. The SCUBA jiggle maps are described in detail in Barger, Cowie, & Sanders (1999), BCR00, and Barger et al. (2001a, b), and the SCUBA raster maps are described in Borys et al. (2002) and C. Borys et al., in preparation. For the jiggle and raster maps, submillimeter fluxes were measured at the positions of the 1.4 GHz ($> 5\sigma$) sources from the catalogs of Richards (2000; HDF-N), E. B. Fomalont et al., in preparation (SSA13), and S. C. Chapman et al., in preparation (SSA22) using beam-weighted extraction routines that include both the positive and negative portions of the beam profile.

Additional targeted SCUBA photometry mode observations were made of the majority of the optically-faint

radio sources over a wider part of the VLA primary beam, including some sources in regions already mapped by SCUBA. The photometry data are described in C01, C02, and S. C. Chapman et al., in preparation. These observations were centered on the radio source coordinates producing a flux measurement at that position. The configuration of the submillimeter data in each of the three fields is depicted in Fig. 1. Of the 278 radio sources in the three fields with submillimeter measurements, all have $850 \mu\text{m}$ flux measurements with uncertainties less than 5 mJy, and of these, 219 have uncertainties less than 2.5 mJy. In total, we significantly ($> 3\sigma$) detect in the submillimeter 50 of the 278 radio sources. Twenty-eight of these lie in the jiggle or raster maps, and 22 are from photometry mode. For reference, there is about one blank sky SCUBA source with > 5 mJy for every 200 SCUBA beams.

3. OPTICAL PROPERTIES AND SPECTROSCOPIC REDSHIFT DISTRIBUTION OF THE MICROJANSKY RADIO SOURCES

Richards et al. (1999) presented the overall I magnitude distribution for the 1.4 GHz and 8.4 GHz samples in the HDF-N and the 8.4 GHz sample in the SSA13 field. They found that the optical counterparts had a wide range of magnitudes with a median $I = 22.1$. The present deeper I -band observations remain consistent with this result. The median I for the HDF-N and SSA13 1.4 GHz sources with I -band measurements is $22.37_{-0.18}^{+0.11}$ (68% confidence). The distribution implies that the bulk of the radio sources (just over 60%) should be bright enough ($I \lesssim 23.5$) for spectroscopic identification. The remaining sources will mostly be too optically faint for spectroscopic identification and will require another method for determining their redshifts.

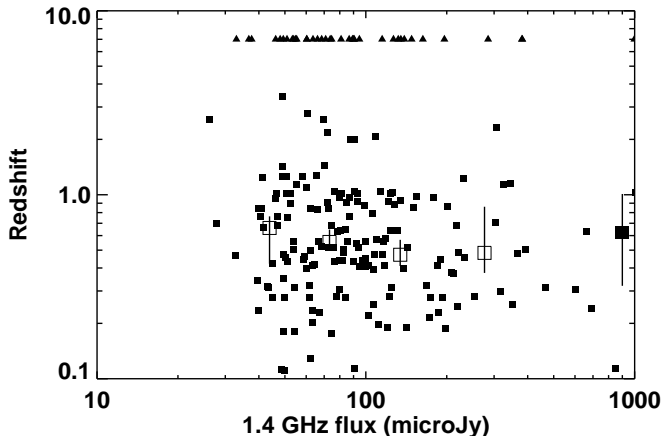


FIG. 2.— Redshift versus 1.4 GHz flux for the spectroscopically-observed radio sources in the HDF-N and SSA13 fields. The solid squares denote sources with redshift identifications, and the solid triangles at $z = 7$ denote sources for which no redshifts could be obtained. The large open squares denote the median redshifts for the identified sources. The 68% confidence range on the median redshifts are indicated by the error bars. The large solid square with error bars shows the median redshift and 68% confidence range of the millijansky radio sample of Waddington et al. (2001).

In Fig. 2 we plot redshift versus $S_{1.4\text{GHz}}$ for the spectroscopically-observed radio sample. Sources with redshifts are denoted by solid squares, and sources for which no redshifts could be obtained are denoted by solid triangles at $z = 7$. The large open squares denote the median redshifts for the identified sources. The median redshift distribution is essentially flat across the entire microjansky regime probed. We also plot the median redshift (large solid square) from a millijansky radio study by Waddington et al. (2001). This point shows a continuation of the flat redshift distribution to brighter radio fluxes. The selection of optically-bright sources inherent in a spectroscopically-identified sample means we are likely missing the high redshift tail of the distribution function. This tail could be skewing to higher redshifts as we move to fainter radio fluxes while the main body of the redshift distribution remains invariant. We shall return to this point when we discuss the submillimeter properties of the radio sources.

In Fig. 3 we plot rest-frame absolute I -band magnitude, M_I , calculated using a standard spiral galaxy K -correction, versus redshift for the spectroscopically-identified radio sources (solid squares). The effect of the $I \sim 23.5$ spectroscopic limit on M_I is indicated by the dashed line, and the effect of our growing incompleteness beyond $I \sim 22$ is indicated by the dotted line. Fig. 3 shows a remarkably narrow range in M_I with redshift (as indicated by the solid lines) that suggests the radio sources are chosen from approximately L^* optical galaxies, regardless of redshift, and the radio hosts are, at a crude level, standard candles in their optical properties. In the redshift range $z = 0.1-0.5$ the mean $M_I = -22.0 \pm 0.9$; for $z = 0.5 - 0.8$ the mean $M_I = -22.6 \pm 0.8$ (by contrast, classical radio galaxies are approximately $5-10 \times L^*$ optical galaxies). As can be seen from Fig. 3, the small increase in absolute magnitude at higher redshifts largely may be due to the apparent magnitude selection effects.

To verify that this result is not an effect of our flux

limited radio sample, we construct a toy model whereby a Schechter luminosity function with $M_I^* = -22.5$ is evolved in luminosity, increasing with redshift as $(1+z)^3$ from $z = 0.1 - 1.5$, and normalized by the volume element, dV . If we were to assume that radio luminosity is proportional to optical (I -band) luminosity, our observed range in M_I would result in only sub- L^* radio sources lying in our sample. However, if we apply our radio flux limit ($\sim 40 \mu\text{Jy}$) to the model, we notice that we can detect only those radio sources with luminosities greater than L^* at all redshifts > 0.3 , with 70% of the detectable sources in the observed volume lying outside of the equivalent M_I range. We conclude that our observed result (microjansky radio sources being hosted by similarly luminous optical galaxies) is not a selection effect of our flux limited radio sample.

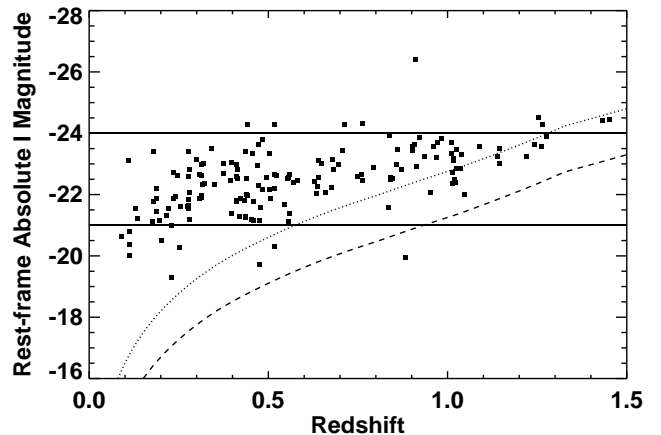


FIG. 3.— M_I versus redshift for the radio sources in the HDF-N and SSA13 fields with spectroscopic redshifts (solid squares). The solid lines show the approximate range in M_I from -21 to -24 where the majority of the sources lie. The dashed line illustrates the effect of an $I \sim 23.5$ spectroscopic limit on M_I , and the dotted line illustrates that of an $I \sim 22$ selection.

It is not clear why the radio sources should all lie in high optical luminosity galaxies. At the higher redshifts the restricted absolute magnitude range can be understood from the selection effects: the lower cut-off is due to low optical luminosity galaxies being faint and not spectroscopically identified, and the upper cut-off reflects the small number of galaxies with optical magnitudes above the optical L^* . However, at the lower redshifts there is no selection against low optical luminosity galaxies, and the absence of these galaxies is striking. Many of the low optical luminosity galaxies at low redshifts have blue colors and substantial ongoing star formation that might be expected to produce substantial synchrotron emission; thus, we might expect this population to correspond to a large part of the radio population. The absence of these objects argues that they are weak in the radio relative to their optical (and ultraviolet) luminosities.

This presumably is the same effect that is seen in the local far-infrared (FIR)-radio correlation, which is not precisely linear; low optical luminosity galaxies have lower radio luminosities than expected (Fitt et al. 1988; Cox et al. 1988; Devereux & Eales 1989). One likely explanation is that small galaxies are not very effective radio sources because cosmic rays are more likely to escape by diffusion or convection (Chi & Wolfendale 1990; Condon et al.

1991.) As our sources are selected from a flux-limited radio survey, low optical luminosity galaxies will be eliminated preferentially from our sample. This is a serious problem for radio estimates of the local star formation rate density (e.g., Mobasher et al. 1999; Haarsma et al. 2000), as a substantial fraction of the ultraviolet luminosity density is generated by faint sub- L^* galaxies at low redshifts (e.g., Cowie, Songaila, & Barger 1999; Wilson et al. 2002). The radio-based star formation rate density estimates already tend to lie at the high end of the values measured in the $z = 0-1$ range, but despite this, the lowest redshift values must be substantially underestimated.

4. SUBMILLIMETER PROPERTIES OF THE MICROJANSKY RADIO SOURCES

In Fig. 4 we plot $S_{850\mu\text{m}}$ versus I -band magnitude for the radio sources with submillimeter measurements, and in Fig. 5 we plot $S_{850\mu\text{m}}$ versus $S_{1.4\text{GHz}}$. The data are divided both according to observation technique (triangles for jiggle map or raster mode, circles for photometry mode) and according to submillimeter detection significance (large solid symbols for $> 3\sigma$, small open symbols for $< 3\sigma$). Analyses of submillimeter source reliability from SCUBA maps suggest a threshold of 4σ (Eales et al. 2000; Scott et al. 2002; Borys et al. 2002; Cowie, Barger, & Kneib 2002); thus, we have enclosed our $> 4\sigma$ sources in a second larger symbol. However, confidence in a targeted submillimeter detection of a known optically-faint radio source is much higher than in a randomly detected submillimeter source. For the 278 radio sources with submillimeter measurements, we expect only 0.5 spurious 3σ sources.

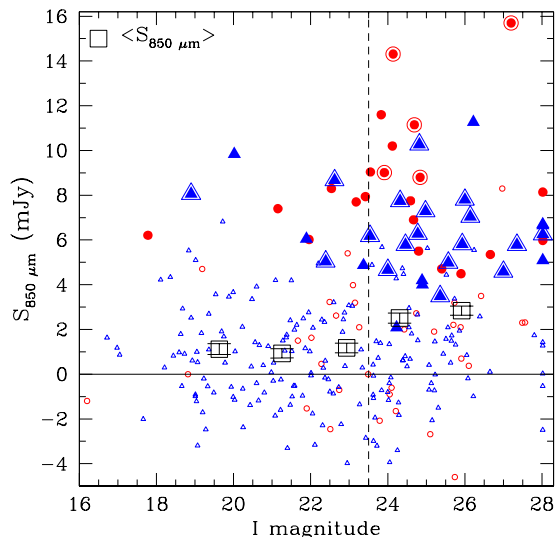


FIG. 4.— Submillimeter flux versus I -band magnitude for the microjansky radio sources in the HDF-N, SSA13, and SSA22 fields with submillimeter measurements. Circles denote SCUBA photometry observations and triangles denote SCUBA jiggle map or raster map observations. Large filled symbols denote sources with $> 3\sigma$ submillimeter fluxes. Sources with $> 4\sigma$ submillimeter fluxes are enclosed in a second larger symbol. The error-weighted mean submillimeter fluxes are shown as large open squares with 1σ uncertainties. The vertical dashed line at $I = 23.5$ shows our division between optically-faint and optically-bright sources. Error bars have not been plotted but are typically ~ 2 mJy.

4.1. Statistical analyses

In Fig. 4 we show the error-weighted mean submillimeter fluxes (open squares with 1σ uncertainties) for five bins of 53 sources at successively fainter I -band magnitudes. The sample as a whole has an error-weighted mean $S_{850\mu\text{m}} = 1.73 \pm 0.09$ mJy. Since the distribution of the noise is not Gaussian (see Cowie, Barger, & Kneib 2002), the computed error may underestimate the true value. However, when Monte Carlo simulations of an equal number of randomly distributed sources are analyzed in the same way, the high significance of the result is confirmed. The optically-faint ($I > 23.5$) subsample is highly significant at 2.37 ± 0.13 mJy, while the optically-bright ($I < 23.5$) subsample is also significant at 1.09 ± 0.13 mJy. Thus, the optically-faint radio sources are about two times more submillimeter luminous, on average, than the optically-bright radio sources. While we have somewhat oversampled the optically-faint radio sources with our targeted submillimeter photometry observations, the result is consistent when we consider only our contiguous submillimeter jiggle map regions.

Both the optically-faint and optically-bright radio-selected samples have higher submillimeter fluxes than X-ray-selected samples: for the 1 Ms *Chandra* Deep Field-North X-ray sample the error-weighted mean $S_{850\mu\text{m}} = 1.21 \pm 0.14$ mJy (Barger et al. 2001b), and for the 75 ks Elais-N2 sample, 1.25 ± 0.40 mJy (Almaini et al. 2002). In fact, Barger et al. (2001b) found that the submillimeter signal of their X-ray sample was largely driven by the subset of sources that overlapped with optically-faint radio sources.

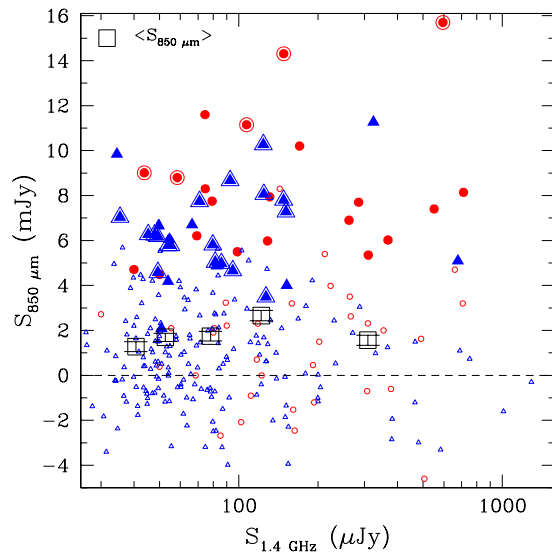


FIG. 5.— Submillimeter flux versus radio flux for the microjansky radio sources in the HDF-N, SSA13, and SSA22 fields with submillimeter measurements. Symbols are as in Fig. 4.

In Fig. 5 we show the error-weighted mean submillimeter fluxes (open squares with 1σ uncertainties) at successively fainter 1.4 GHz fluxes. The mean rises (from $S_{850\mu\text{m}} \sim 1$ mJy to 3 mJy) with increasing radio flux out to about $100 \mu\text{Jy}$ before dropping to $S_{850\mu\text{m}} = 1.2$ mJy for the brightest radio sources. For radio fluxes approaching the millijansky regime, we expect an increasing contribu-

tion from active galactic nuclei (AGN). This appears to be reflected in the trend of the means: the brightest radio sources in our sample are, on average, not the strongest submillimeter emitters (luminous AGN typically have low $S_{850\ \mu\text{m}}/S_{1.4\ \text{GHz}}$ ratios). Since the SSA13 radio image is deeper than the HDF-N and SSA22 images, the number of radio sources probed in the submillimeter is not simply proportional to the radio source counts. However, the statistics should not be affected by this, unless significant large-scale structure dominates the small field covered to this depth. Note that within the area probed by our submillimeter observations, only two radio sources have radio fluxes higher than 1 mJy.

4.2. Direct submillimeter source detections

Fifty of the radio sources in our sample are significantly ($> 3\sigma$) detected individually in the submillimeter. Of these, 38 fall into the optically-faint ($I > 23.5$) region of Fig. 4, which is consistent with the conclusion of previous SCUBA surveys that most submillimeter sources are optically faint (e.g., BCR00; Smail et al. 2002; C01). The percentage of $S_{850\ \mu\text{m}} > 5\ \text{mJy}$ ($> 3\sigma$) submillimeter sources detected in our survey versus optical brightness is presented in Table 1; the radio selection technique becomes highly efficient for optical magnitudes fainter than $I \sim 24$.

While the submillimeter detection rate of $I < 23.5$ radio sources is rather poor, this population still makes up a fraction of our submillimeter sample. To quantify this, we consider only regions of our survey that were mapped with SCUBA to avoid the bias introduced by the optically-faint criterion used for the targeted photometry follow-up. Using our combined jiggle and raster maps of the three fields, we find that 20 of the submillimeter-detected sources have $I > 23.5$ and 9 have $I < 23.5$. Thus, $69 \pm 9\%$, where the errors correspond to the 1 sigma variance in the expectation value, of the radio-submillimeter population has $I > 23.5$. This appears to be inconsistent with the claim by Ivison et al. (2002), based on a smaller sample, that the bulk of the radio-detected submillimeter sources are optically bright.

4.3. Overlap of the bright submillimeter population with the microjansky radio population

Using our jiggle and raster mapped regions ($> 300\ \text{arcmin}^2$), we can determine what fraction of bright submillimeter sources are picked out by an ultradeep radio sample. As the radio properties in the SSA22 field are highly non-uniform due to bright radio sources, we again restrict our analysis to the HDF-N and SSA13 fields. We also restrict to $> 4\sigma$ sources with $S_{850\ \mu\text{m}} > 5\ \text{mJy}$. We have adopted an $8''$ search radius to avoid missing associations due to the positional uncertainties of the $S/N \sim 4$ SCUBA detections. Note that the $8''$ search radius should not give rise to any spurious associations as the surface density of radio sources is only $\sim 2\ \text{arcmin}^{-2}$ in the central regions of our maps. We find that $66 \pm 7\%$ of bright submillimeter sources (29 of the $N \sim 4$ SCUBA detections) have radio identifications. This is consistent with Ivison et al. (2002), who found that 18 of the 30 submillimeter sources in their sample have radio identifications, which translates to a percentage of $60 \pm 9\%$. From § 4.2, about 70% of these counts will be picked out by the optically-faint radio sources.

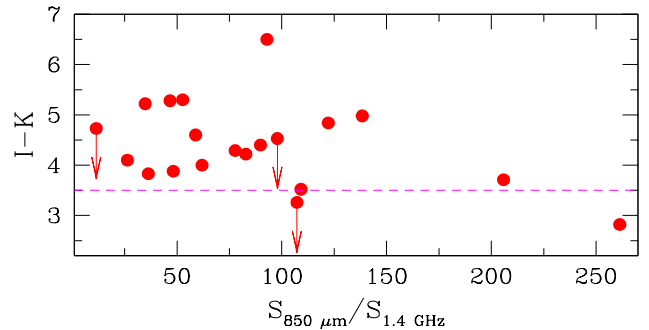


FIG. 6.— $I - K$ versus the ratio of submillimeter to radio flux for the microjansky radio sources in the HDF-N and SSA22 fields with both submillimeter and K -band measurements. Sources with marginal K -band detections are shown as 3σ upper limits. The dashed line shows the Very Red Object limit, $I - K = 3.5$.

4.4. $I - K$ Colors

We have K -band measurements for a subset of our radio sample. Both the optically-bright and optically-faint radio subsamples have significantly redder $I - K$ colors than the field galaxy population. The optically-faint radio sources show a monotonic trend to redder colors (Richards et al. 1999; BCR00): at $I = 22$, median $I - K = 2.9$ and at $I = 24.5$, median $I - K = 3.4$. For comparison, the field galaxy sample has median $I - K \sim 2$ at $I \sim 22$ and median $I - K \sim 2.3$ at $I \sim 24.5$ (e.g., Barger et al. 1999).

In Fig. 6 we plot $I - K$ versus $S_{850\ \mu\text{m}}/S_{1.4\ \text{GHz}}$ for the 3σ submillimeter-detected radio sources with K -band measurements. All of the sources have I -band detections, but three of the sources are only marginally detected at K and are shown as 3σ upper limits. The submillimeter-detected sources have median $I - K = 4.3$ and median $K = 20.7$. From Fig. 6 we can see that a color cut of $I - K > 3.5$ includes 95% of the submillimeter-detected sources. This is consistent with the results of Wehner, Barger, & Kneib (2002), who used a submillimeter survey of three massive cluster fields to determine that the median submillimeter source has $K = 20 - 20.3$, depending on the cluster sample used, and that $I - K > 3.5$ sources (Very Red Objects) contribute about two-thirds of the $850\ \mu\text{m}$ extragalactic background light.

There is no obvious trend of $I - K$ color with $S_{850\ \mu\text{m}}/S_{1.4\ \text{GHz}}$ in Fig. 6, implying that the near-infrared colors of the submillimeter-selected galaxies are insensitive to redshift over the $z = 1-3$ range as would be expected if the red colors are primarily caused by dust extinction.

5. MILLIMETRIC REDSHIFT ESTIMATION FOR THE MICROJANSKY RADIO-SELECTED SAMPLE

5.1. Evolution of the radio population with redshift

The radio power of the spectroscopically-identified sample in the HDF-N and SSA13 fields is shown in Fig. 7, where we have computed the radio K -correction assuming a synchrotron spectral index of -0.8 . The selection limits of the HDF-N and SSA13 samples ($40\ \mu\text{Jy}$ and $25\ \mu\text{Jy}$, respectively) are shown by the solid curves. The conversion to FIR luminosity, computed using the local FIR-radio correlation (e.g., Condon 1992), is shown on the right-hand axis, and the dotted and dashed lines show the FIR luminosity limits for luminous infrared galaxies (LIGs) and

ultraluminous infrared galaxies (ULIGs), respectively.

There is a rapid evolution in the upper bound of the radio power. This is the well-known effect that large galaxies at $z \sim 1$ frequently have very large star formation rates while at lower redshifts the rates turn down rapidly (Cowie et al. 1996, where the phenomenon is called downsizing). An equivalent description is that near-ULIGs or ULIGs are extremely rare at low redshifts, but the number density rises rapidly with redshift so that they are relatively common by $z = 1$ (e.g., Blain et al. 1999; BCR00). In combination with the lower-bound selection imposed by the flux limits, this effect means that we have a rapidly changing but rather well-defined population with redshift. At low redshifts ($z < 0.4$) we are selecting Milky Way type galaxies, at intermediate redshifts we are selecting LIGs, and at $z > 1$ we are selecting only near-ULIGs or ULIGs.

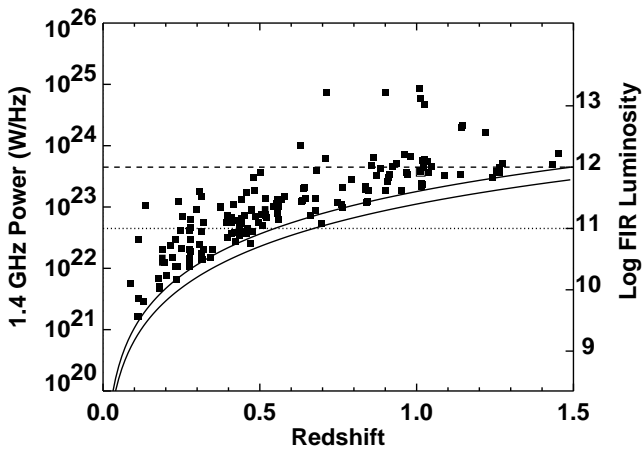


FIG. 7.— Radio power versus redshift for the radio sources in the HDF-N and SSA13 fields with spectroscopic redshifts. The solid curves show the selection limits for the two fields ($40 \mu\text{Jy}$ and $25 \mu\text{Jy}$, respectively). The right vertical axis shows the logarithm of the FIR luminosity (in solar luminosities) that would be inferred from the radio power, based on the local FIR-radio correlation. The FIR luminosity limits of LIGs ($10^{11} L_{\odot}$) and ULIGs ($10^{12} L_{\odot}$) are shown by the dotted and dashed lines, respectively.

5.2. Average $S_{850 \mu\text{m}}/S_{1.4 \text{GHz}}$ flux ratios

Our present dataset enables us to determine the normalization with redshift of the error-weighted mean $S_{850 \mu\text{m}}/S_{1.4 \text{GHz}}$ flux ratio. In Fig. 8 we plot the logarithm of the error-weighted mean $S_{850 \mu\text{m}}/S_{1.4 \text{GHz}}$ for the radio sources with spectroscopic redshifts and submillimeter measurements (large open squares). The four $> 3\sigma$ submillimeter-detected sources with redshifts (see § 5.3) are shown as dots. We include on the figure the tracks with redshift for three spectral energy distributions (SEDs) with different dust properties: Arp 220 (short dashed), a typical *IUE* starburst (solid), and a Milky Way type galaxy (dotted). We have calculated these tracks using the Dale et al. (2001) and Dale & Helou (2002) empirical SED library. We also include three tracks from the literature (DCE00; CY00; Yun & Carilli 2002) that were derived using different galaxy samples and assumptions; these tracks are the most widely used in millimetric redshift estimation. As would be expected from the luminosity selection, the error-weighted means follow the track of a quiescent to moderately star-forming galaxy at lower redshifts, while at higher redshifts the observations migrate to values 10

below the Arp 220 and CY00 tracks. (We note that Yun, Reddy, & Condon (2001) found that sources like Mrk 231, whose AGN has a radio luminosity comparable to its starburst luminosity, likely constitute a few to 10% of the submillimeter population. Such sources may lie preferentially in our radio-selected sample and hence have lowered our high-redshift ULIG points by about 0.3 in dex.)

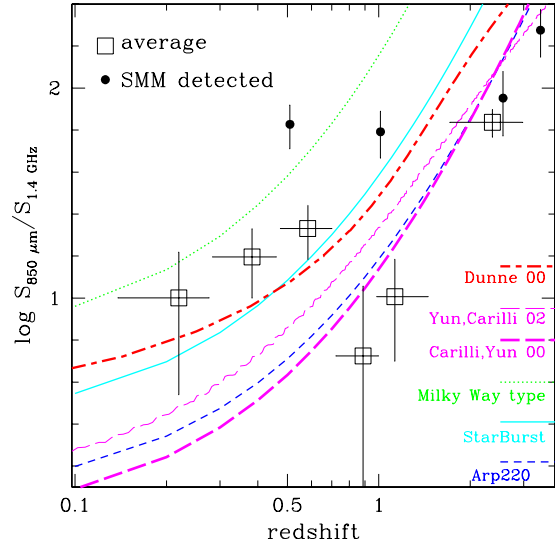


FIG. 8.— $\log S_{850 \mu\text{m}}/S_{1.4 \text{GHz}}$ versus redshift for the microjansky radio sources with spectroscopic redshifts and submillimeter measurements. Squares denote the error-weighted means in six equal-number bins. The four $> 3\sigma$ submillimeter-detected sources with reliable redshifts are shown as dots. The tracks are Arp 220, a Milky Way type galaxy, a typical *IUE* starburst, and Dunne et al. (2000), Carilli & Yun (2000), and Yun & Carilli (2002).

The radio power and the FIR luminosity correlate locally with dust temperature, and there is no evidence that this relation varies significantly with redshift (Chapman et al. 2003, Blain, Barnard & Chapman 2003). Given this, the evolution in radio power and in $S_{850 \mu\text{m}}/S_{1.4 \text{GHz}}$ with redshift show that for the microjansky radio population, millimetric redshift estimates at low redshifts are best made with a template intermediate between a Milky Way type template and a starburst template, and those at high redshifts ($z > 1$) with an Arp 220 template. Thus, we can apply the millimetric redshift technique to other radio-submillimeter populations *provided* we have knowledge of the characteristic FIR luminosity or redshift of the population before we choose a template SED.

In Fig. 3 we showed that nearly all radio sources with redshifts have similar M_I . This suggests that the optically-faint radio sources, rather than being low optical luminosity galaxies at moderate redshifts are instead luminous galaxies at $z > 1$, where the negative *K*-correction in the submillimeter provides a nearly one-to-one mapping of submillimeter flux to submillimeter luminosity. For the sources that are individually detected in the submillimeter, the $S_{850 \mu\text{m}}$ fluxes (see Fig. 4) give FIR luminosities that are at least as large as Arp 220 ($> 10^{12} L_{\odot}$). We therefore can use the Arp 220 template in making millimetric redshift estimates for the optically-faint microjansky sources.

In Fig. 9a we show $S_{850 \mu\text{m}}/S_{1.4 \text{GHz}}$ versus 1.4 GHz flux. The right-hand vertical axis shows the redshift that would be inferred from the Arp 220 template. In Fig. 9b we

divide the sample into optically-bright and optically-faint subsamples. We can see from this figure that the optically-faint subsample does indeed move to higher redshift as we probe to fainter radio fluxes.

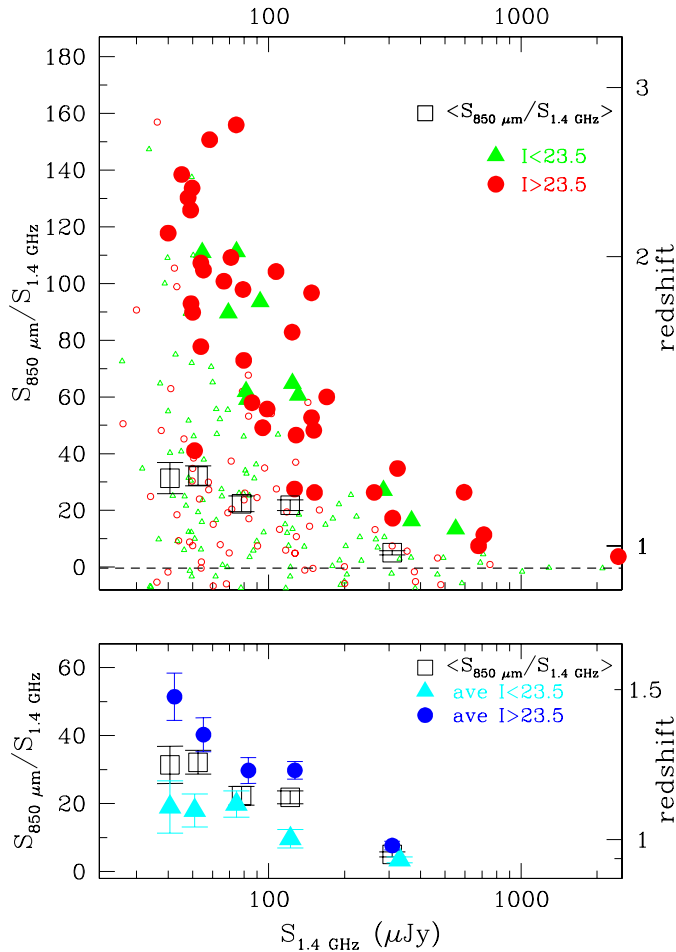


FIG. 9.— (a) $S_{850\ \mu\text{m}}/S_{1.4\ \text{GHz}}$ versus 1.4 GHz flux for the microjansky radio sources in the HDF-N, SSA13, and SSA22 fields with submillimeter measurements. Large filled symbols denote sources with $> 3\sigma$ submillimeter fluxes. Triangles (circles) denote sources with $I < 23.5$ ($I > 23.5$). Assuming the sources span a reasonably small range in dust temperature and properties, the y-axis can be interpreted as a redshift measure (right-hand scale). The redshift range covered by our radio sources is $z \sim 0 - 3$ for typical dust temperatures encountered in local starburst galaxies and ULIGs. The mean $S_{850\ \mu\text{m}}/S_{1.4\ \text{GHz}}$ is independent of radio flux for sources fainter than about $200\ \mu\text{Jy}$, within 1σ statistical errors. (b) Mean $S_{850\ \mu\text{m}}/S_{1.4\ \text{GHz}}$ versus 1.4 GHz flux for the optically-bright and optically-faint subsamples. The nearly constant $S_{850\ \mu\text{m}}/S_{1.4\ \text{GHz}}$ ratio of the total sample is dominated by the optically-bright sources.

5.3. Individual sources

There are four significant ($> 3\sigma$) submillimeter sources in our sample with spectroscopic redshifts ($z = 3.405$, $z = 2.565$, $z = 1.013$, and $z = 0.510$); all have $I < 23.5$. The $z = 3.405$ source has Lyman α and CIV in emission, and the $z = 2.565$ source is a broad-line quasar that was detected in the 100 ks *Chandra* exposure of the SSA13 field (Barger et al. 2001a). The redshifts of both sources are very close to their millimetric redshift estimates. The $z = 1.013$ source shows strong Balmer absorption features and [Ne III] in emission and was detected in the 1 Ms

Chandra Deep Field-North exposure (Barger et al. 2001b). The spectroscopic redshifts of this and the $z = 0.510$ source are lower than their millimetric redshift estimates (assuming an Arp 220 SED, we find $z = 1.6$ and $z = 1.9$, respectively). Sources with dust temperatures cooler than the Arp 220 ~ 45 K template will have true redshifts and FIR luminosities lower than predicted (see also Yun & Carilli 2002). The $z = 1.013$ galaxy exhibits a cool dust temperature (~ 30 K), similar to recently identified cold ULIGs from the FIRBACK $170\ \mu\text{m}$ ISOPHOT survey (Chapman et al. 2002c). In the case of the $z = 0.510$ galaxy, however, the dust would have to be prohibitively cold (~ 18 K) for the millimetric redshift to match the spectroscopic identification. This source may therefore be a misidentification, with the true source being lensed by the bright foreground galaxy (Chapman et al. 2002b).

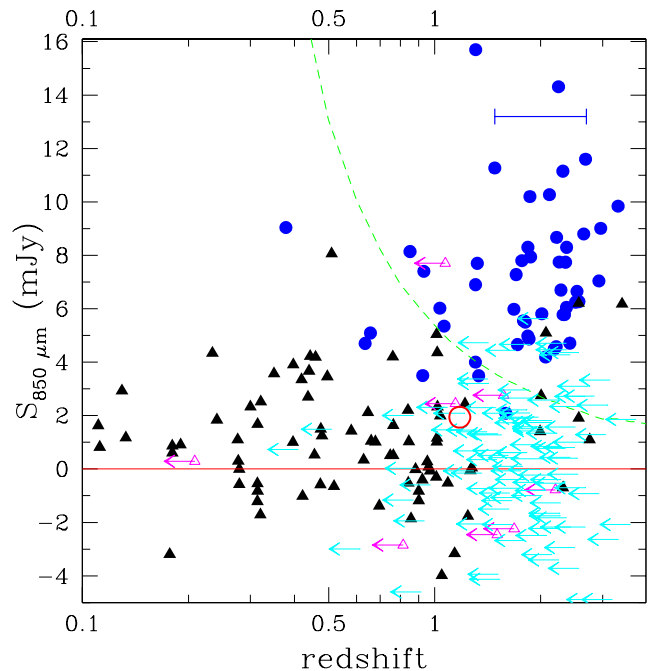


FIG. 10.— Submillimeter flux versus redshift for the microjansky radio sources with submillimeter measurements. The $I < 23.5$ sources with (without) spectroscopic redshifts are denoted by solid (open) triangles, and the $I > 23.5$ sources with submillimeter detections (and hence millimetric redshifts) are denoted by solid circles. The sources without $> 3\sigma$ submillimeter detections are denoted by left-pointing arrows at the millimetric redshift limit (estimated using the 2σ submillimeter uncertainty) and the measured $S_{850\ \mu\text{m}}$ flux. The error-weighted mean $S_{850\ \mu\text{m}}/S_{1.4\ \text{GHz}}$ of these sources is denoted by a large open circle at its millimetric redshift estimate of $z = 1.13$. The track of a galaxy twice as luminous as Arp 220 is shown as a dashed line. The expected characteristic error at $z = 2$, based on the range in properties for local ULIGs relative to the Arp 220 template, is indicated by a horizontal bar.

5.4. Combined spectroscopic and millimetric redshift sample

In Fig. 10 we plot $S_{850\ \mu\text{m}}$ versus spectroscopic (solid triangles) or millimetric (solid circles) redshift for the sources with submillimeter measurements. We also show a rough error bar based on the range in properties for local ULIGs relative to the Arp 220 template. We have very little information on the spectroscopically-undetected radio sources that are not individually detected in the submillimeter. We can put conservative limits on their redshifts by esti-

mating millimetric redshifts from the CY00 relation and the 2σ submillimeter uncertainty. We denote these sources by the left-pointing arrows in Fig. 10.

We can go one step further by determining a single average point for this marginally detected population from the ratio of the error-weighted mean submillimeter flux and the error-weighted mean radio flux. We denote this point by a large open circle at $z = 1.13$ on Fig. 10. As we have already removed all the $S_{850\ \mu\text{m}} > 3\sigma$ sources, submillimeter sources without radio counterparts are not present. Since the steep submillimeter source counts imply a large Eddington bias, it is important not to overinterpret this result, but we note that it falls naturally within the distribution of the more robustly identified sources.

Comparing the data with the track followed by a ULIG with twice the luminosity of Arp 220 (dashed line in Fig. 10), we can see the rapid rise in luminous FIR sources with increasing redshift. Below $z \sim 1$ there are essentially no such objects, while above $z \sim 1$ they are common.

SUMMARY

We presented optical and submillimeter (jiggle and raster maps and photometry) imaging and optical spectroscopy for a sample of microjansky radio sources detected in ultradeep 1.4 GHz maps of the HDF-N, SSA13, and SSA22 fields. Our spectroscopic identifications for 169 of the sources in the HDF-N and SSA13 fields revealed a flat median redshift distribution across the entire microjansky regime probed. The identified sources show a remarkably narrow range in rest-frame absolute I -band magnitude that suggests they are chosen from approximately L^* optical galaxies, regardless of redshift. At the higher redshifts the narrow range can be understood from selection effects, but at the lower redshifts there is no selection against low optical luminosity galaxies. Thus, the absence of low optical luminosity galaxies in the sample argues that they are weak in the radio relative to their optical and ultraviolet luminosities, possibly due to small galaxies not being efficient at retaining the cosmic rays necessary to host microjansky radio sources. The fact that these galaxies are eliminated preferentially from a flux-limited radio survey poses a serious problem for radio estimates of the local star formation rate density since a substantial fraction of the ultraviolet luminosity density is generated by sub- L^* galaxies at low redshifts.

From a statistical analysis of our submillimeter measurements for 278 of the microjansky radio sources in the HDF-N, SSA13, and SSA22 fields, we found that optically-faint radio sources are about three times more submillimeter luminous, on average, than optically-bright radio sources, but both populations are, on average, very significantly detected in the submillimeter. Fifty of the radio sources in our sample are significantly ($> 3\sigma$) detected individually in the submillimeter; 38 of these are optically faint ($I > 23.5$). We have spectroscopic redshifts for four of the $I < 23.5$ submillimeter-detected sources, three of which are in the range $z = 1\text{--}3.4$; the fourth source is at $z = 0.510$ and may be a misidentification.

To quantify the percentage of optically-bright and optically-faint radio sources that are significantly detected in the submillimeter, we considered only the regions of our survey that were mapped with SCUBA (as opposed to the regions that were targeted with photometry). We

found that $69 \pm 9\%$ of the radio-submillimeter population has $I > 23.5$. We also found that $66 \pm 7\%$ of the $S_{850\ \mu\text{m}} > 5\text{ mJy}$ ($> 4\sigma$) sources in our fields are radio-identified.

We used our spectroscopically-identified microjansky radio sample to determine the evolution with redshift in the radio power and hence the FIR luminosity (through the FIR-radio correlation). We found that ULIGs or near-ULIGs are extremely rare at low redshifts but are relatively common by $z = 1$. In combination with the lower-bound selection effects, this means that we have a population which is rapidly changing with redshift but that is fairly tightly selected at each redshift. At low redshifts ($z < 0.4$) we are selecting Milky Way type galaxies, at intermediate redshifts we are selecting LIGs, and at high redshifts ($z > 1$) we are selecting only ULIGs or near-ULIGs. From the error-weighted mean $S_{850\ \mu\text{m}}/S_{1.4\ \text{GHz}}$ flux ratio we see the same evolution with redshift, such that at lower redshifts the error-weighted means follow the track of a quiescent to moderately star-forming galaxy, while at higher redshifts the observations migrate to values consistent with Arp 220. Thus, millimetric redshift estimates at low redshifts are best made with a template intermediate between a Milky Way type template and a starburst template, while at high redshifts ($z > 1$) an Arp 220 template is appropriate. With this knowledge, we estimated millimetric redshifts or limits for all of the optically-faint microjansky radio sources in our sample with submillimeter measurements.

We thank an anonymous referee for helpful comments that improved the manuscript. We thank Ian Smail for a careful reading of a draft of the paper and for useful discussions. We gratefully acknowledge support from NASA through grant 9174 (SCC) and DF1-2001X (LLC), from the University of Wisconsin Research Committee with funds granted by the Wisconsin Alumni Research Foundation (AJB), and from NSF grants AST-0084847 (AJB) and AST-0084816 (LLC). DS and CB are supported by the Natural Sciences and Engineering Research Council of Canada.

REFERENCES

- Almaini, O., et al., 2002, MNRAS, submitted (astro-ph/0108400)
- Barden, S. C., Armandroff, T., Muller, G., Rudeen, A. C., Lewis, J., & Groves, L. 1994, in "Instrumentation in Astronomy VIII", eds. D.L. Crawford and E.R. Craine, Proc. SPIE Vol. 2198, p. 87
- Barger, A. J., Cowie, L. L., Sanders, D. B., Fulton, E., Taniguchi, Y., Sato, Y., Kawara, K., & Okuda, H. 1998, Nature, 394, 248
- Barger, A. J., Cowie, L. L., & Sanders, D. B. 1999, ApJ, 518, L5
- Barger, A. J., Cowie, L. L., Trentham, N., Fulton, E., Hu, E. M., Songaila, A., & Hall, D. 1999, AJ, 117, 102
- Barger, A. J., Cowie, L. L., & Richards, E. A. 2000, AJ, 119, 2092 (BCR00)
- Barger, A. J., Cowie, L. L., Mushotzky, R. F., & Richards, E. A. 2001a, AJ, 121, 662
- Barger, A. J., Cowie, L. L., Steffen, A. T., Hornschemeier, A. E., Brandt, W. N., & Garmire, G. P. 2001b, ApJ, 560, L23
- Barger, A. J., Cowie, L. L., Brandt, W. N., Capak, P., Garmire, G. P., Hornschemeier, A. E., Steffen, A. T., & Wehner, E. H. 2002, AJ, in press (astro-ph/0206370)
- Blain, A. W., Jameson, A., Smail, I., Longair, M. S., Kneib, J.-P., & Ivison, R. J. 1999, MNRAS, 309, 715
- Blain, A. W., Barnard, V., Chapman, S. 2003, MNRAS, in press (astro-ph/0209450)
- Borys, C., Chapman, S. C., Halpern, M., & Scott, D. 2002, MNRAS, 330, L63
- Bridger, A., et al. 2000, in "Advanced Telescope and Instrumentation Control Software", eds. H. Lewis, Proc. SPIE Vol. 4009, p. 227
- Carilli, C. L. & Yun, M. S. 1999, ApJ, 513, L13 (CY99)
- Carilli, C. L. & Yun, M. S. 2000, ApJ, 539, 1024 (CY00)
- Chapman, S. C., Richards, E.A., Lewis, G. F., Wilson, G., & Barger, A. J. 2001, ApJ, 551, L9 (C01)
- Chapman, S. C., Lewis, G. F., Scott, D., Borys, C., & Richards, E.A. 2002a, ApJ, 570, 557 (C02)
- Chapman, S. C., Smail, I., Ivison, R. J., & Blain, A. W. 2002b, MNRAS, in press (astro-ph/0204086)
- Chapman, S. C., Smail, I., Ivison, R. J., Helou, G., Dale, D., Lagache, G. 2002c, ApJ, 573, 66
- Chapman, S. C., Helou, G., Lewis, G., & Dale, D. A. 2003, ApJ, submitted, (astro-ph/0211xxx)
- Chi, X., & Wolfendale, A. W., 1990, MNRAS, 245, 101
- Cohen, J. G., Hogg, D. W., Blandford, R., Cowie, L. L., Hu, E., Songaila, A., Shopbell, P., & Richberg, K. 2000, ApJ, 538, 29
- Condon, J. J., Anderson, M. L., & Helou, G. 1991, ApJ, 376, 95
- Condon, J. J. 1992, ARA&A, 30, 575
- Cowie, L. L., Songaila, A., Hu, E., & Cohen, J. 1996, AJ, 112, 839
- Cowie, L. L., Songaila, A., & Barger, A. J. 1999, AJ, 118, 603
- Cowie, L. L., Barger, A. J., & Kneib, J.-P. 2002, AJ, 123, 2197
- Cox, M. J., Eales, S., Alexander, P., & Fitt, A. J. 1988, MNRAS, 235, 1227
- Cuillandre, J.-C., Luppino, G. A., Starr, B. M., & Isani, S. 2000, in "Optical and IR Telescope Instrumentation and Detectors", eds. M. Iye and A. F. Moorwood, Proc. SPIE Vol. 4008, p. 1010
- Dale, D. A., Helou, G., Contursi, A., Silbermann, N. A., & Kolhatkar, S. 2001, ApJ, 549, 215
- Dale, D. A. & Helou, G. 2002, ApJ, 576, 159
- Devereux, N. A. & Eales, S. 1989, ApJ, 340, 708
- Dunne, L., Clements, D. L., & Eales S. A. 2000, MNRAS, 319, 813 (DCE00)
- Eales, S., Lilly, S., Webb, T., Dunne, L., Gear, W., Clements, D., & Yun, M. 2000, AJ, 120, 2244
- Fitt, A. J., Alexander, P., & Cox, M. J., 1988, MNRAS, 233, 907
- Haarsma, D. B., Partridge, R. B., Windhorst, R. A., & Richards, E. A. 2000, ApJ, 544, 641
- Hodapp, K.-W., et al. 1996, NewA, 1, 177
- Holland, W. S., et al. 1999, MNRAS, 303, 659
- Hughes, D. H., et al. 1998, Nature, 394, 241
- Ivison, R. J., et al., 2002, MNRAS, in press (astro-ph/0206432)
- Miyazaki, S., Sekiguchi, M., Imi, K., Okada, N., Nakata, F., & Komiyama, Y. 1998, in "Optical Astronomical Instrumentation", ed. S. D'Odorico, Proc. SPIE Vol. 3355, p. 363
- Mobasher, B., Cram, L., Georgakakis, A., & Hopkins, A. 1999, MNRAS, 308, 45
- Oke, J.B., et al. 1995, PASP, 107, 375
- Richards, E. A., Fomalont, E. B., Kellermann, K. I., Windhorst, R. A., Partridge, R. B., Cowie, L. L., & Barger, A. J. 1999, ApJ, 526, L73
- Richards, E. A. 2000, ApJ, 533, 611
- Sanders, D.B. & Mirabel, I.F. 1996, ARA&A, 34, 749
- Smail, I., Ivison, R. J., Owen, F. N., Blain, A. W., & Kneib, J.-P. 2000, ApJ, 528, 612
- Smail, I., Ivison, R. J., Blain, A. W., & Kneib, J.-P., 2002, MNRAS, 331, 495
- Scott, S., et al. 2002, MNRAS, 331, 817
- Waddington, I., Dunlop, J. S., Peacock, J. A., & Windhorst, R. A. 2001, MNRAS, 328, 882
- Wehner, E. H., Barger, A. J., & Kneib, J.-P. 2002, ApJ, in press
- Wilson, G., Cowie, L. L., Barger, A. J., & Burke, D. J., AJ, 124, 1258
- Windhorst, R. A., et al. 1995, Nature, 375, 471
- Yun, M. & Carilli, C., 2002, ApJ, 568, 88
- Yun, M., Reddy, N., & Condon, J. 2001, ApJ, 554, 803

TABLE 1
 AVERAGE SUBMILLIMETER FLUXES FOR THE HDF-N+SSA13+SSA22 SAMPLE IN I -MAGNITUDE BINS

I -mag Bin	$S_{850\ \mu\text{m}}$ (mJy)	σ_{850} (mJy)	number in bin	% SMM detections ($> 3\sigma$)
$I > 25$	2.38	0.18	68	26%
$24 < I < 25$	2.85	0.23	43	37%
$23 < I < 24$	1.32	0.27	32	24%
$22 < I < 23$	1.00	0.28	36	8%
$21 < I < 22$	1.13	0.26	31	9%
$19.5 < I < 21$	1.10	0.31	31	3%
$I < 19.5$	1.08	0.29	37	5%